

Understanding the role of glaze layer with aligned images from multiple surface characterization techniques

Chuchu Zhang^{a,*}, Richard W. Neu^{a,b}

^a School of Materials Science and Engineering, Georgia Institute of Technology, Atlanta, GA, 30332, USA

^b George W. Woodruff School of Mechanical Engineering, Georgia Institute of Technology, Atlanta, GA, 30332, USA



ARTICLE INFO

Keywords:

Glaze layer
High-temperature wear
Image analysis
Computer vision
Fretting

ABSTRACT

A glaze layer that significantly reduces friction and wear has been found on the surface of many Fe-, Cr-, and Ni-based material systems undergoing fretting/sliding at elevated temperature. In this paper, we propose a novel way to understand the role of glaze layer using computer vision algorithms. Two workflows, one for quantitative glaze layer identification and the other for image alignment, have been developed. For glaze layer identification, we used computer vision concepts that considers the color and reflection of glaze layer under optical microscope (OM). For image alignment, we developed a strategy to conduct pixel-to-pixel alignment of images acquired by multiple techniques (e.g., OM, scanning electron microscopy, 3D optical profilers) with sub-pixel error. As such, the correlation between the height map and locations of the glaze layer within the wear scar can be readily determined. These methods are used to evaluate wear scars generated on 310S stainless steel under like-on-like, cylinder-on-flat fretting conditions from 20 °C to 700 °C. The glaze layer is found to always occupy relatively high locations within wear scar. With temperature rise, the projected coverage of glaze layer follows the same increasing trend with three distinguishable stages, and the threshold temperature of the three stages matched with severe-to-mild wear transition. These results provide evidence that severe-to-mild wear transition resulted from spreading of glaze layer coverage, and glaze layer may reduce friction and wear by reducing real contact area.

1. Introduction

A severe-to-mild wear regime transition has been observed in many Fe-, Cr-, and Ni-based alloys after fretting/sliding in oxygen-containing atmosphere with increasing of ambient temperature [1–6]. It is believed that this transition is caused by the development of a wear-resistant tribo-layer, namely “glaze layer”, at the contact interface. Once formed, the glaze layer will act as a load-bearing layer and significantly reduce friction and wear from then on. It is critical to understand the nature of glaze layer to understand its role in friction and wear reduction, which makes it possible to use this understanding to motivate future mechanical design of wear resistant interfaces.

One of the most recognized hypotheses that explain the wear resistant nature of glaze layer is that the glaze layer helps to reduce or eliminate the metal-on-metal contact of the two bodies [7–9]. At the same time, the greater hardness and good high temperature ductility of the glaze layer makes it more wear resistant than the substrate material [10–13]. Several hypotheses have also been proposed to predict the

timing at which the glaze layer is readily developed at a given working condition, for example, glaze layer reaching a critical thickness [14,15] or critical cycle [5,16]. While these studies provide valuable insights on our understanding of glaze layers, most of the characterization has involved either highly localized imaging (i.e., high magnification) or homogenized measures such as the change in contact resistance between the two bodies.

Since the measured coefficient of friction and wear volume depend on the entire surface in contact, knowing the glaze layer distribution within the wear scar is important. The coverage of glaze layer within the contact area needs to be sufficient to achieve the severe-to-mild transition. In fact, it has been reported that small patches of glaze layer are present before the severe-to-mild transition finishes [17].

Studying the distribution of glaze layer within wear scar is indeed a challenging task, because the surface height profile itself does not incorporate the chemical or mechanical property information that could be used to distinguish the glaze layer. One solution is to bring in other characterization techniques that are capable to identify the glaze layer.

* Corresponding author.

E-mail address: zhcc09@gatech.edu (C. Zhang).

Success of this strategy requests both high-quality alignment and precise identification of glaze layer and its boundary.

The prior requirement can be easily fulfilled if the multiple spectrums are collected by one characterization tool, as such the signals are by nature perfectly aligned. In 1997, Jiang et al. [18] built an adapted 3-dimensional contact profiler that measures contact resistance between the sample surface and the metal stylus simultaneously during scanning of surface profile. Because the glaze layer has high concentration of oxide and thus high electrical resistance, the glaze layer region can be recognized by its high electrical resistance. By comparing the glaze layer coverage to the tribological test results at various temperatures, the authors found that the critical projected coverage of glaze layer upon finishing of severe-to-mild wear transition is less than 50%, and the glaze layer formation is preferable in the central area of the wear scar. However, the resolution of this set up (about 130 μm) is too low to precisely detect boundary of glaze layer. Like most contact mode surface profilers, this method has a physical limitation on the resolution by the tip size and the density of the scanning trace mesh. In addition, it is challenging for this method to differentiate between non-glaze oxide layer (i.e., static oxide layer) formed at extreme temperatures and the glaze layer itself. Therefore, this work did not lead to meaningful conclusion for height distribution of glaze layer.

In fact, the second requirement of precisely identifying the glaze layer and its boundary is not a trivial task. In much of the literature, the glaze layer identification is purely based on a descriptive criteria such as “shiny, smooth, highly oxidized, compacted, superficial layer” as defined when the concept was first coined [19]. Because quantitative description of glaze layer is missing, glaze layer identification for most studies [1,10,11,16,20–22] have been purely qualitative. This limitation further leads to the difficulty of effectively defining the boundary of the glaze layer. It is not a big issue for local probing type of research that only examine a small portion within glaze layer under high magnification observation, but it matters when it comes to large scale statistical analysis on glaze layer, for example, the distribution of glaze layer.

Herein, we aim to address the challenge of studying the distribution of glaze layer with a novel strategy that meets both alignment and resolution requirements. For alignment, instead of seeking equipment that can do-it-all, we take advantages of several individual characterization tools, each of which captures some aspect of glaze layer’s characteristics, and align the resulting images from each tool by computer vision principles. With help of Vickers hardness indentation markers as fiducial points, good alignment has been achieved with sub-pixel error. This methodology can be used to integrate as many surface mapping spectrums as necessary (e.g., OM, scanning electron microscopy, 3D optical profilers, nano-hardness map, etc.). For precise glaze layer identification, we proposed a novel quantitative criterion based on optical microscope (OM) images of wear scars with a specific lighting mode. Optical microscopy is a rapid, easily accessible and cost-effective equipment for worn surface characterization. It can achieve high resolution in large range of magnification, which makes it feasible to characterize wear scars from a wide variety of contact configuration and test conditions. The proposed criteria are tested and validated by comparing to scanning electron microscope (SEM) images.

This paper will start with introducing basic computer vision concepts used in this work that may be unfamiliar to the wear community. Section 3 will briefly describe the tribological tests conducted to generate the wear scars we studied in this work. In section 4, the role and specific settings of three characterization tools, namely, OM, SEM, and optical profilometer, will be described. Their resulting images are aligned for integration of the information and glaze layer identification. After glaze layer regions are segmented, the distribution of glaze layer within wear scar as a function of environmental temperature is discussed in two perspectives: projected glaze coverage from top-view, and height variation of glaze layer from vertical perspective. The results provide evidence that the glaze layer is facilitated at relative high location within wear scar, which decreases friction and wear by reducing the real

contact area during fretting/reciprocating sliding.

2. Background

2.1. Homography transformation

A homography transformation describes the geometric relation between two individual 2D images of the same planar object [23]. It is a common technique used in the field of computer vision. Considering two images that are taken by two different cameras of one planar object, a point on image 1 with coordinate (x_1, y_1) and a point on image 2 (x_2, y_2) that correspond to the same physical point of the planar object must have the following relation:

$$\begin{bmatrix} x_1 \\ y_1 \\ 1 \end{bmatrix} = H_t \begin{bmatrix} x_2 \\ y_2 \\ 1 \end{bmatrix} \quad (1)$$

where H_t is a 3 by 3 matrix that defines the homography transformation. Although H_t has 9 elements in total, it has only 8 degree of freedom to enforce the constraint that the third element of the resulted vector is always 1. Given the property that a homography transformation has 8 degree of freedom, we can compute the homography transformation between an image pair with a minimal four pairs of known (x_1, y_1) and (x_2, y_2) that correspond to the four physical points, i.e., fiducial points, on the same plane [23]. More pairs of fiducial points are desired to reduce stochastic error when calculating the H_t matrix. In such over-constrained situation where more than four pairs of matched points are provided, an optimal solution of H_t can be calculated with least square method.

Once the homography matrix H_t is calculated, it can be used to find any corresponding point from one image to another, and the image 2 can be transformed to image 2' that is aligned with the reference image, image 1.

2.2. HSV color space and its separation

HSV (Hue, Saturation, Value) is an alternative representation of more commonly used RGB (Red, Green Blue) color space. It describes all colors in a cylindrical geometry: Hue (H) is the angular dimensions, representing the true color in a circle (0° - red, 120° - green, 240° - blue and 360° back to red); Saturation (S) is the distance to the central vertical axis, and it represents the amount of color presented in percentage of pure color (full saturation); Value (V) is the central vertical axis that corresponds to the intensity scaling, or brightness. Both V and S are in the interval $[0,1]$. H is in the interval $[0^\circ, 360^\circ]$ [24]. An example of an image after HSV separation can be founded in Fig. 1.

3. Wear tests

The fretting wear tests characterized in this work were conducted on hot rolled and annealed 310S stainless steel (Penn Stainless Products, USA) with composition given in Table 1. The wear test configuration was cylinder-on-flat, with the contact configuration shown in Fig. 2, using the same stainless steel for both bodies. The dimensions of cylindrical samples (denoted as the pin) and the flat specimens (denoted as the plate) along with the test parameters provided in Table 1. The work hardening layer on the plate samples was removed by polishing up to 4000 grit, and the pin samples were used as machined by CNC lathing. The tests were conducted on a DN55 high temperature fretting and reciprocating sliding test system (Phoenix Tribology, UK). In this setup, the pin sample oscillates vertically at commanded displacement amplitude(δ) and frequency(f), and the two plate samples are stationary. The normal force P is applied by a pneumatic actuator with feed-back control from an inline load cell. Additional details on the testing procedures can be found elsewhere [25].

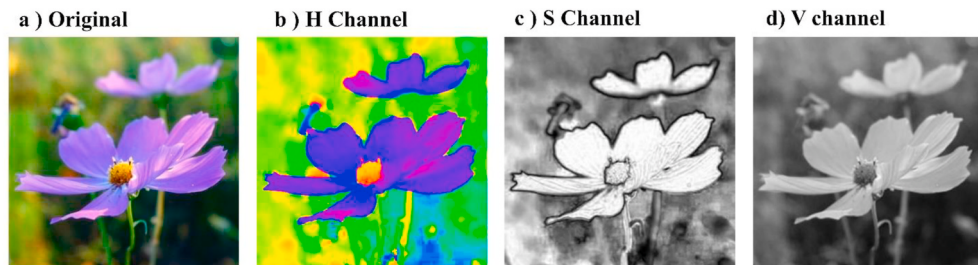


Fig. 1. Example of conducting HSV color space separation for a photograph of flowers: a) Original image; b) H channel; c) S channel; d) V channel. H channel are colored to better illustrate the color ($S = V = 1$). (For interpretation of the references to color in this figure legend, the reader is referred to the Web version of this article.)

Table 1

Fretting wear test parameters. Material composition is from vendor supplied datasheet. Yield strength and Young's modulus measured from tensile specimens extracted from the 310S plate material.

Chemical composition (wt%)	24.49%Cr, 19.95%Ni, 1.49%Mn, 0.16%Mo, 0.41%Cu, 0.46%Si, 0.028%P, Fe balance
0.2% Yield strength (MPa)	283(20 °C), 231(200 °C), 218(400 °C), 150(600 °C), 124(800 °C)
Youngs modulus (GPa)	173(20 °C), 168(200 °C), 146(400 °C), 134(600 °C), 100(800 °C)
Normal force (N)	150
Applied amplitude (μm)	±200
Frequency (Hz)	10
Contact length (mm)	13
Cylinder radius (mm)	10
Temperature (°C)	20 °C, 100 °C, 200 °C, 250 °C, 280 °C, 300 °C, 400 °C, 500 °C, 600 °C, 700 °C
Cycles	66000

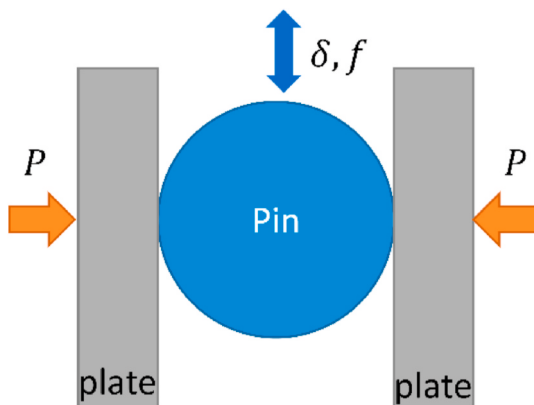


Fig. 2. Schematic of the contact configuration.

The stabilized Coefficient of friction (Cof) at the end of each wear test at each temperature is shown in Fig. 3(a). The Cof is calculated based on the root mean square of the real time tangential force. The evolution of Cof with cycle at three selected temperatures is shown Fig. 3(b). The averaged Cof beyond 40 K cycle is considered the stabilized Cof for each test. The wear loss is evaluated by net wear volume, calculated by subtracting volume up (volume above unworn reference plane, positive value) from volume down (volume below unworn surface, positive value), of each cleaned pin-plate pair after the fretting wear test. The net wear volume for each temperature is also reported in Fig. 3(a) with reversed axis. For each temperature, at least three duplicate wear tests were conducted.

The Cof and net wear volume performance of the 310S–310S couple shows four distinguishable stages that presents a severe wear to mild wear transition. Both Cof and net wear volume was relatively high at temperatures below 200 °C (Region I), with the maximum net wear volume being about -1.3 mm^3 at 200 °C. Severe-to-mild wear transition occurs between 200 °C and 300 °C (Region II), where the Cof and net wear volume loss decrease dramatically as the influence of the glaze

layer formed at the interface gradually takes place. In the mild wear region (Region III), net volume loss is nearly two magnitudes smaller than that at 200 °C and almost negligible due to the full glaze layer protection. With further increases in temperature (Region IV) to the highest temperatures considered, 600 °C–700 °C, the Cof shows an increasing trend again and positive net wear volume is observed (i.e., more volume gain than loss). The increasing of Cof may result from severe plastic deformation of the two bodies due to the reduced yield strength of the substrate, further enhanced adhesion between the like bodies and wear debris, or possible local welding occurring before the start of the test. The positive net wear volume likely results from extensive oxidation and local welded wear debris near the edge of the wear scar due to enhanced adhesion and diffusion. The evolution of Cof at 280 °C, 500 °C and 700 °C shown in Fig. 3 (b) are typical representations of Region II, Region III and Region IV, respectively. In contrast to rapid reduction of the Cof at 500 °C and 700 °C (less than 5000 cycles), at 280 °C it took more cycles to reach a stabilized low Cof. This result implies that glaze layer formation at the lower temperature requires more time, which is consistent with the recently proposed critical glaze layer formation cycle, N_{gl} model [17]. It also worth noting that the “transition” between severe wear and mild wear in this work mostly considers the wear volume and Cof change. Since wear volume can only be readily measured accurately at the end of the test, severe wear, mild wear, and the transition region are identified based on the final wear volume. The possible dynamic wear mechanism change during the process of one specific test is not specifically studied in this work since it will require conducting multiple tests under the same conditions interrupting at different cycle counts. Overall, we expect that Region II will minimally shift to lower temperatures as the cycle count is increased based on the N_{gl} model.

4. Characterization of wear scars and demonstration of workflows

Samples after 250 °C, 280 °C, 300 °C, 400 °C, 500 °C, 600 °C, and 700 °C fretting test were used to study the differences in the glaze layer characteristics with temperature. After the tests, loose debris were

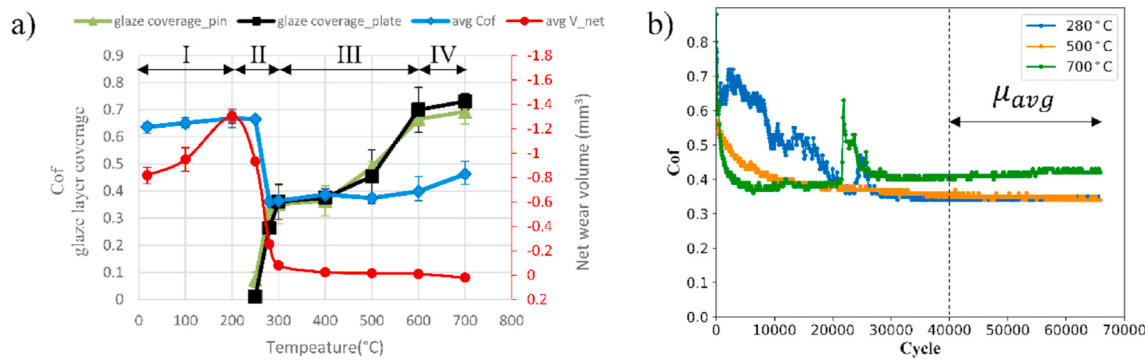


Fig. 3. (a) Effect of temperature on wear volume (net volume loss), average coefficient of friction (Cof) and glaze layer coverage on pin and plate. (b) Evolution of the coefficient of friction with cycle for 280 °C (transition zone), 500 °C (glaze protection zone) and 700 °C (local welding zone) test.

cleaned in alcohol using an ultrasonic bath. For each pair of pins and plates, a 2.5 mm section was randomly selected along the total 13 mm contact length of the wear scar. Fiducial markers were made with a Vickers hardness tester (Mitutoyo HM-200, Tokyo, Japan). The fiducial markers were placed in an unworn area near the selected section of wear scar on plates, and they were used as reference for the homography transformation to align images acquired from different methods. To achieve the preferred marker size (50–100 µm in diagonal for current set up), 0.5-1kgf load was chosen based on hardness of the samples. Redundant markers were applied for convenience of later point matching steps. To minimize error of H_t calculation, it is ideal to spread markers over the four corners of the rectangular view of aligned image.

4.1. Characterization tools

The marked surface is characterized by optical microscope (OM), scanning electronic microscope (SEM) and optical profilometer for reflection, color, chemical composition, and height information.

4.1.1. Optical microscope (OM)

Optical microscope images were taken with Leica DVM6 (Wetzlar, Germany) in Z-stack mode that overlap focused images with height variance. 20% intensity of Coaxial illumination (CXI) and 10% intensity of Ring Lightning (RL) mode were used together for lightening at full aperture to highlight glaze layer and its boundaries in OM images. Schematics of the different lighting modes and their resulting OM images of the same wear scar can be found in Fig. 4. Among the two lighting sources, CXI is the more critical one providing a strong, concentrated, and vertical incident light. As shown in Fig. 4(b), the glaze layer will stand out with strong reflection due to its flat and smooth surface morphology. At the same time, the boundary of glaze layer patches will be clearly outlined. The RL lighting mode, on the other

hand, involves a ring of lighting source and the incident light is slightly divergent. As a common lighting mode that is available in most OM equipment, RL mode by itself (Fig. 4(a)) does not highlight glaze layer as good as CXI. However, the additional RL light to the CXI mode (Fig. 3(c)) can help to enhance the reflection of the wear trace on glaze layer, and thus improve the accuracy of glaze layer detection. The circled area in Fig. 4(b) and (c) serves as a demonstration of such improvement.

All OM images used in this work were taken at the same white balance, lighting intensity and saturation so that any color and brightness difference between images are only caused by the surface characteristics of the wear scar, not the OM settings.

4.1.2. SEM

SEM images were acquired using the Hitachi SU-8230 (Tokyo, Japan) with cold field emission gun in either secondary electron (SE) or backscatter electron (BSE) modes using 20 KeV and 20 mA. The SE signal is sensitive to surface morphology, where darker regions represent smooth surfaces. In contrast the BSE signal highlights the elemental component information, where features with lighter elements appear darker in the BSE images. Since the glaze layer is a smooth and highly oxidized layer, it is expected to appear dark in both SE and BSE images.

4.1.3. Optical profilometer

The optical profilometer used in this work, Zygo Zegage 3D optical profilometer (Middlefield, CT, USA), is a non-contact surface profiler based on the principle of two-beam interferometry [26]. The output of the optical profilometer is a height map of the surface profile scanned. Since 10X lens and 1X zoom was the only option available with our instrument, stitching mode (20% overlap) was used to cover a 3486 µm × 2882 µm rectangular area for all specimens. This rectangular area covers a selected region of wear scar, fiducial markers, and part of the surrounding unworn surface on both sides of the wear scar in the

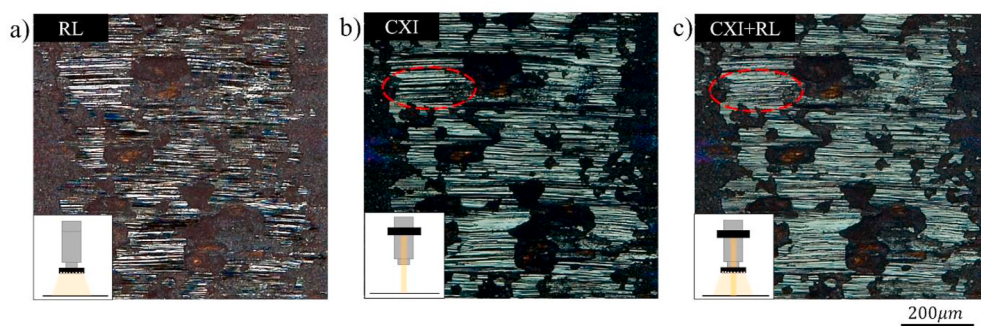


Fig. 4. Schematic of different lighting mode and their resulting OM image at the same view of wear scar after 500 °C test: a) with ring lighting (RL) mode, 60% intensity; b) with coaxial illumination (CXI) mode, 20% intensity; c) with combined CXI (20% intensity) and RL lighting mode (10% intensity). The three OM images share the same scale bar.

reciprocating direction. Using the Zygo software Mx (version 7.5.0.1), the average height of unworn surface is defined as the reference (i.e., denoted as zero height) to correct the tilt of the specimen and/or the scanning platform, and the scan voids are filled by data interpolation. The lateral resolution (defined as the minimal distinguishable height difference between neighboring camera pixels) of the Zygo is 0.815 μm .

4.2. Image alignment workflow

The general idea of image alignment is to calculate a ground truth homography transformation matrix H_t , and then apply this matrix H_t to align an image with the reference image. This process is achieved using a home-built Python script with OpenCV library. As an illustrative example, OM-height map alignment for a plate tested at 280 °C is used to demonstrate the workflow. The original height map and OM image is shown in Fig. 4(a) and (b), respectively. The height map is colored by assigning overall maximum height in red and minimum height in blue of the scanned area.

Before starting the process, the reference image is selected. In this work, the height map is chosen as reference image and therefore, the OM image is aligned to the height map. This arrangement is made for two reasons: Firstly, it can unify magnification of all OM images. The magnification of the profilometer is fixed, while the OM images could be acquired at various magnifications to compensate for width variations in the wear scar to achieve the best resolution. Secondly, the height map is a tilt-corrected image using the software of the optical profiler. Consequently, using the height maps as alignment reference can correct all OM images to the same tilt-removed perspective.

The first step of image alignment is to calculate the H_t matrix. For this purpose, more than 8 pairs of fiducial points, i.e., the center of

Vickers indentation scars, were matched between the two images, Fig. 5 (a) and Fig. 5(b). To improve labeling accuracy of this step, the pre-selected areas in the height map and OM image that contain each pair of indentation scars are magnified, and the pre-selected area of the height map is temporarily re-colored to enhance image contrast to assist in center identification of the indentation scars. Fig. 5(c) and (d) demonstrate one pair of such magnified area of the original height map and the OM image as the dashed blocks marked in Fig. 5(a) and (b). The center of the red crosses is the labeled fiducial point that represent the center of the same indentation scar.

Among the matched points pairs, the majority (6 or more pairs) were used to calculate a tentative homography transformation matrix H_t , while the remaining pairs are used to estimate the error of this H_t matrix. If the error is less than 1 pixel, this H_t matrix is finalized as the ground truth matrix H_t ; otherwise, the manual matching process is repeated until sub-pixel error is obtained.

Afterwards, the H_t matrix is applied to the OM image to align it with the height map. After alignment, the aligned OM image and the height map share a same dimension and same pixel resolution (up to 0.73 μm). In this example and many other cases where the magnification of the original OM image is higher than that of the height map, a compensated blank area will appear at the edges of the aligned OM image (e.g., Fig. 5 (e)). A subsequent edge trimming is applied to the aligned images to remove the blank areas. The final output height map and OM image pair is shown in Fig. 5(f) and (g).

4.3. Glaze layer identification workflow with H-V criterion

In this work, we proposed a new and quantitative criterion, called the H-V criterion, to segment the glaze layer portion from the general

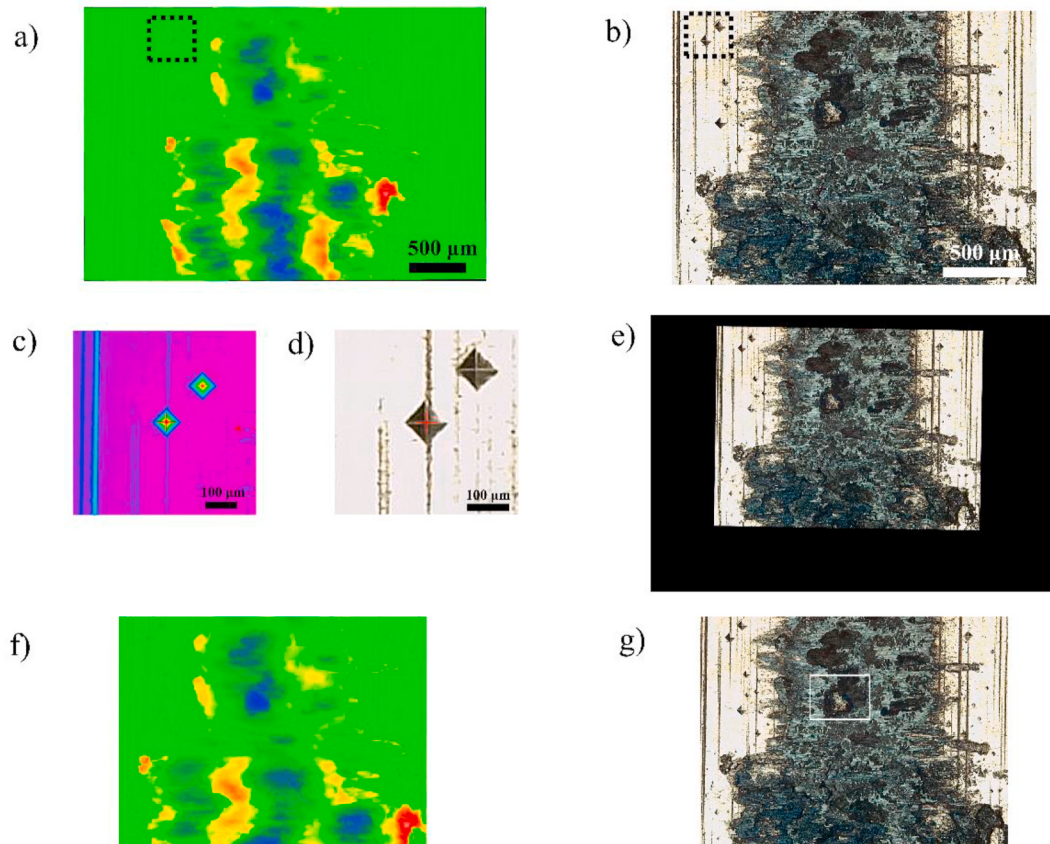


Fig. 5. Outcome images of image alignment workflow demonstrated with images of 280C plate: (a) Original height map; (b) Original OM; (c) magnified and recolored marker area in height map; (d) magnified marker area in OM; (e) aligned OM image; (f) final height map; (g) final aligned OM. (a) and (e)–(g) share the same scale bar. The region selected by white frame in (g) is used for validation of glaze layer identification criteria in section 5.1.

wear scar area in an OM image. Using this criterion, we can identify glaze layer with the fewest sample preparation steps and a single tool, optical microscope. While qualitatively identifying the glaze layer through optical imaging is common practice, the H-V criterion provides the means to convert the assessment of a human tribology expert into a quantitative criterion that a computer can understand and execute automatically.

An example of this glaze layer identification workflow in given in Fig. 6. As discussed earlier, the glaze layer and its boundaries can be highlighted by CXI lighting mode with high brightness due to its smooth surface morphology. The glaze layer portion always appears a blue-green color under our optical microscope. The color characteristics were found to be independent of test temperature, which will be discussed later in the results section. Furthermore, the brightness and color information can be extracted from an image using its Value (V) and Hue (H) channels, respectively, after conducting the HSV separation. Therefore, the two characteristics of a glaze layer, color and brightness (or level of reflection) under optical microscope observation, can be quantitatively translated to two requirements to form the H-V criterion:

H-requirement: its color should fall in a hue range from H_{min} to H_{max} ;

V-requirement: its brightness should be no smaller than a minimum V value, V_{min} .

A pixel i with (H_i , V_i) hue and value is labeled as glaze layer only if both H and V requirements are met, i.e.

$$\begin{cases} H_{max} \geq H_i \geq H_{min} \\ V_i \geq V_{min} \end{cases} \quad (2)$$

The three parameters: V_{min} , H_{min} and H_{max} are adjusted to correctly label the glaze layer that has been recognized during SEM observation for calibration. Additional discussion of turning these parameters using SEM image as a reference can be found in section 5.1. In this specific example, the values of these parameters are: $V_{min} = 0.35$, $H_{min} = 56$, $H_{max} = 169$. The filtered result for H or V requirement is a binary mask, called the H mask or V mask. Every pixel that meets the criteria, Eq. (2), is labeled as '1', or white, in the binary mask image; otherwise, the pixel is '0' or black. Boolean intersection operation is then applied to the H and V mask image to find the locations where pixels meet both requirements, and those pixels are labeled as glaze layer. The binary image made up by the glaze layer pixels are called a raw glaze layer mask. In practice, wear traces on top of glaze layer that are parallel to the sliding direction can be misjudged as "non-glaze layer" using this algorithm due to its low reflection. This error is reduced by adding a small portion of RL lightning to enhance the reflection, and by applying opening/closing operation [27] to fill the remaining uncaptured traces on glaze layer. As the final output, the output glaze layer mask is saved.

Since no spatial transformation was applied in this workflow, the input and output image (and all other intermediate images) are by nature of the same dimension and perfectly aligned with each other. Furthermore, if the input OM image has been pre-aligned with its pairing height map, the resulting binary mask will be aligned with the height map as well. This way the height information of wear scar is fused

with the glaze layer mask, which enables statistical analysis of height distribution on the glaze layer and non-glaze layer individually.

5. Results and discussion

5.1. Application and evaluation of the H-V criterion

To verify the feasibility of proposed H-V criterion and get its optimized parameters H_{min} , H_{max} , V_{min} , SE and BSE SEM images were used to compare with the glaze layer identification obtained from the OM image. As an example, Fig. 7 demonstrates the validation process for the plate tested at 280 °C. Due to the limitation of the minimum magnification of our SEM, a small portion of the wear area was used for the validation. To have an intuitive judgment on the accuracy of glaze layer identification, the SE SEM image is overlaid with the glaze layer identified from the OM image (shadowed in red) in Fig. 7 (g). This overlay is achieved by aligning the OM image to the SE SEM image (Fig. 7 (f)) following the workflow introduced in Section 4.2, and by applying the H-V criterion on the aligned OM image (Fig. 7(a)). The only difference is that there is no Vickers indentation fiducial mark within the field of observation. In this special case, local characteristics, such as small islands, sharp corners, etc., are chosen as fiducial points for alignment. The identified glaze layer portion, highlighted in red in Fig. 7(g), shows good agreement with the glaze layer confirmed by the SEM image, and confirmed that H-V criterion worked very well in precisely identifying glaze layer and its boundary.

In this example, we also noticed a special area, identified as "shiny spot" in the view of observation. As indicated in the V-channel image of OM (Fig. 7(b)), this area has high brightness, and the brightness of its center is even higher than that of a general glaze layer. However, the shiny spot area is judged as non-glaze layer because it fails the H requirement. This judgment made by the H-V criterion is supported by SEM observations. In the SE SEM image (Fig. 7(f)), the shiny spot area has similar gray level to that of glaze layer, meaning its morphology is relatively flat (and thus has high V value in OM image). However, its BSE SEM image is much brighter comparing to that of glaze layer area, indicating the elements in the shiny spot are heavier, and thus contains a reduced oxygen component. This observation is further confirmed by point EDS analysis (20 keV, 20 mA). Three locations were examined, one in the glaze layer, one in the shiny spot, and one in the reference area outside of wear scar. The average weight percentage of major elements and their standard deviations are summarized in Table 2. Comparing to the glaze layer area, the oxygen detected in the shiny spot area is one magnitude smaller. The chemical composition in shiny spot area is very close to the reference area where a static oxide layer was formed. Moreover, the color of the shiny spot in the OM image is also similar to that of the unworn area. In fact, such high brightness shiny spot has been observed at other temperature. The specific color of the shiny spot in the OM images varies at different testing temperature, either similar to the reference area or to the color of stainless steel that was tempered at slightly lower temperature. It is then hypothesized that the shiny spot

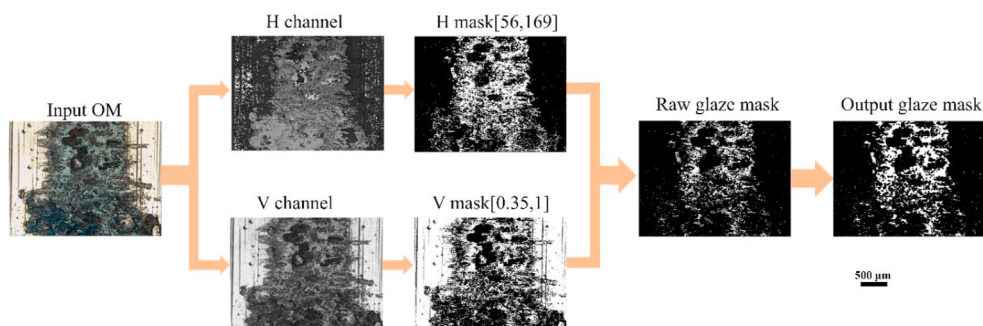


Fig. 6. Glaze layer identification workflow for an OM image acquired from a plate that experienced fretting at 280 °C. All images share the same scale bar.

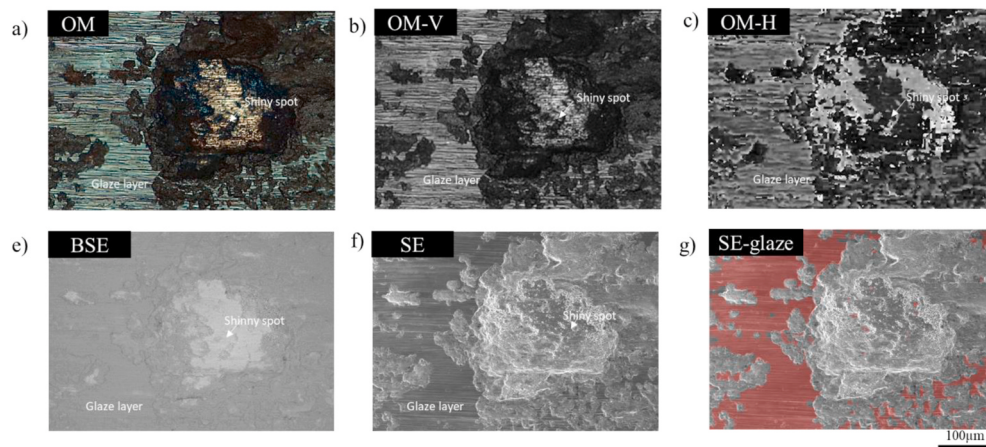


Fig. 7. Demonstration of identifying glaze layer with OM image with reference of SEM, OM is pre-aligned to SE SEM: a) OM image; b) Value channel of OM; c) Hue channel of OM; d) BSE SEM image; e) SE SEM image; f) SE SEM overlaid with glaze layer mask (shaded in red) identified from OM. All images share the same scale bar. (For interpretation of the references to color in this figure legend, the reader is referred to the Web version of this article.)

Table 2

Point EDX analysis on major elements in glaze layer, shiny spot and reference area, all results are in wt%.

Major Elements	Glaze layer	Shiny spot	Reference
O	22.2 ± 3.0	1.4 ± 0.3	2.0 ± 1.0
Cr	20.4 ± 1.0	26.7 ± 0.2	25.5 ± 0.2
Fe	41.4 ± 1.7	52.1 ± 0.3	50.0 ± 2.1
Ni	14.6 ± 0.3	18.7 ± 0.3	18.2 ± 0.7

area may be a thin static oxide layer formed at freshly exposed surface near the end of the test or during the cooling period right after the test finished. The flatness of this area may be caused by surface rubbing as implied by the observed wear trace along fretting direction on top of it. Therefore, the shiny spot should be excluded from the glaze layer category.

To summarize, the comparison of independent identifications of the glaze layer between OM and SEM images suggests that the H-V criterion works well, and neither of its two requirements, H-requirement or V requirement, is redundant.

It is worth noting that the specific number for brightness and color of an OM image can be greatly influenced by light intensity and OM camera setting, especially the white balance setting. In this study, all lighting

and camera settings were fixed. Calibration will be needed to compare results taken by different optical microscopes and cameras. Fig. 8 shows the three parameters used to analyze the OM images of samples tested at different temperatures. The reference color and brightness at each H and V value are provided along the side axes. Interestingly, the H value of the glaze layer area always ranges from about 60° to 180°, which falls in the green spectrum, regardless of the testing temperature. Nevertheless, the average H value for glaze layer area is very stable (around 106°) across all testing temperatures. Similarly, V_{min} for all samples is about 0.33. The fact that the glaze layer hue always falls in a certain range of color may not be coincident. If we consider the thin film interference theory, this result may imply that glaze layer formed at the given testing condition has a certain similar thickness or composition that is independent of temperature. These hypotheses need to be tested by a quantitative study on glaze layer thickness, and additional analysis on wear scars of other materials whose glaze layer have different chemical composition.

5.2. Height distribution for glaze layer at different temperature

Having completed the alignment of the height map, OM image and its glaze layer identification mask, every pixel in the height map is labeled as either “glaze layer” or “non-glaze layer”. The height information of glaze layer and non-glaze layer can now be easily extracted

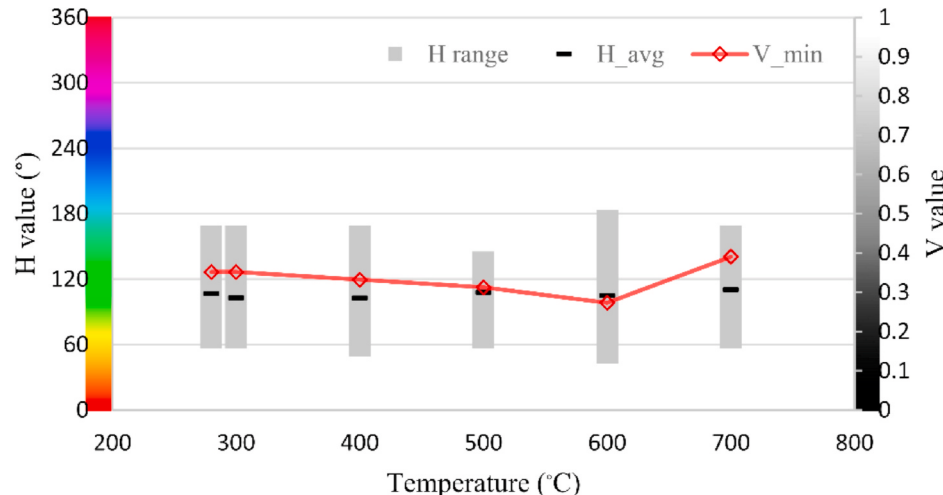


Fig. 8. Hue range (Lower end = H_{min} , upper end = H_{max}) and V_{min} parameter used to identify glaze layer at each testing temperature, overlapped with average Hue value of glaze layer area(H_{avg}).

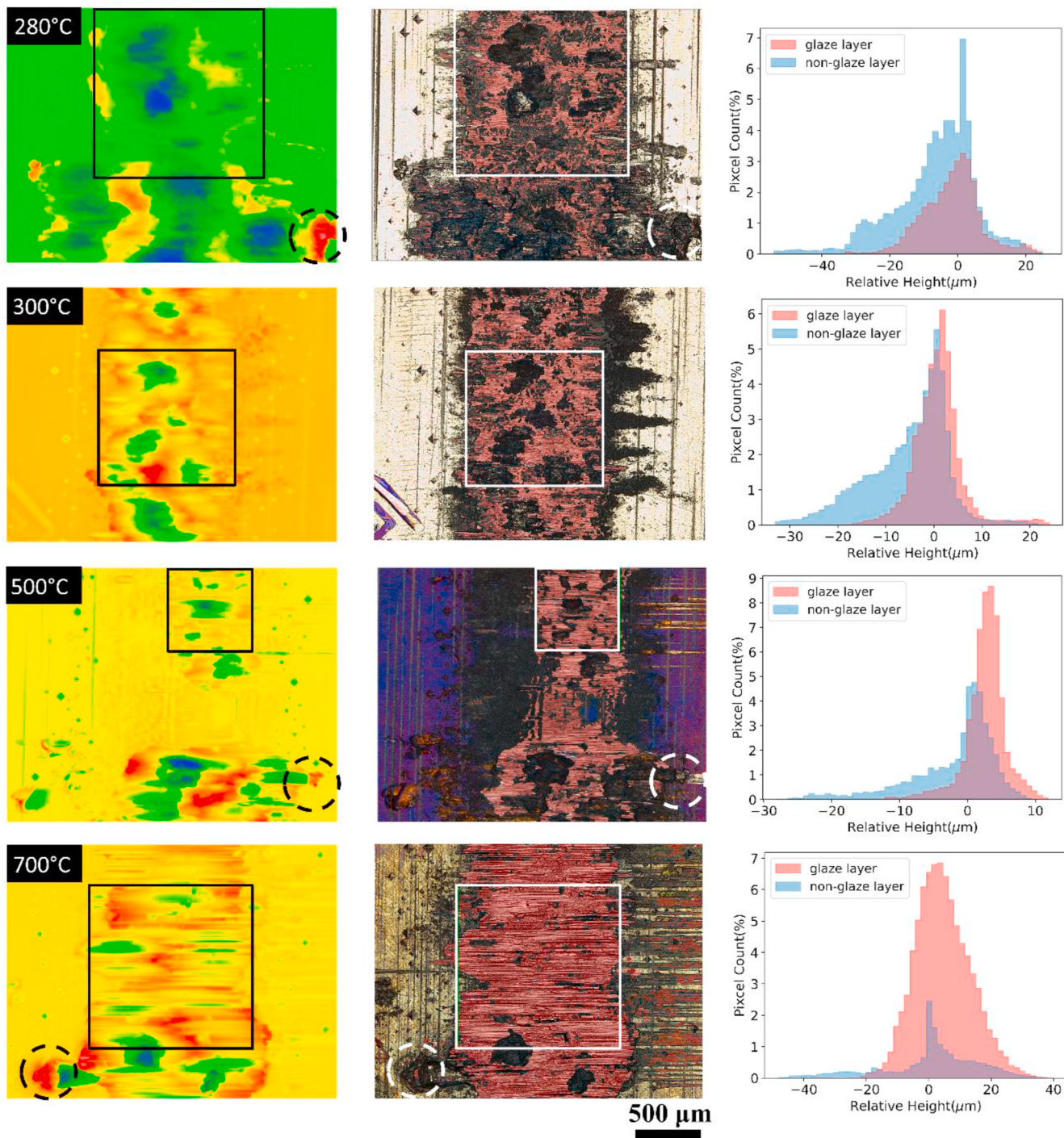


Fig. 9. Histogram of height for glaze layer and non-glaze layer area and their fitted Gaussian distribution curve at 280 °C, 300 °C, 500 °C and 700 °C (right column). The overlaid square in height map (left column) and OM (middle column) represented the sampling location of the data subsets for each sample. Typical build-ups at the edge of wear scar are circled in dashed line. All OM images and height maps share the same scale bar.

and studied from a statistical perspective.

The right column of Fig. 9 summarizes the typical height distribution of glaze layer and non-glaze layer at different temperatures that are within and beyond the severe-to-mild wear transition temperature range in 50 bins histograms. The locations of the data subsets used in each histogram are identified by the white or black squares overlayed on corresponding OM images (the middle column) and height maps (the left column), respectively. The y axis in the histogram is the normalized pixels count, calculated by the pixel count of glaze layer or non-glaze layer pixel for each bin divided by the total number of pixel in the

selected area. The relative vertical location between the glaze and non-glaze histogram suggests that glaze layer tends to have greater height compared to the non-glaze layer. This trend is further confirmed by comparing the mean (μ) height of the glaze and non-glaze layers of each dataset in Table 3, that the glaze layer has higher average height than the non-glaze layer for all temperatures tested. Regarding the height variation, the tighter distribution of both the glaze and non-glaze height histogram from 280 °C to 500 °C suggests that the height variation for both the glaze and non-glaze layers is reduced, indicating a shallower and smoother wear scar at higher temperature. At extreme temperatures

Table 3

Mean (μ), standard deviation (σ) and hypothesis test results for height distribution of glaze and non-glaze layer at each temperature.

Sample	μ_{glaze} (μm)	$\mu_{\text{non_glaze}}$ (μm)	σ_{glaze} (μm)	$\sigma_{\text{non_glaze}}$ (μm)	t value	p value
280C_plate	-1.722	-6.530	8.711	12.138	-95.340	<0.001
300C_plate	0.797	-5.203	5.110	8.442	-140.693	<0.001
400C_plate	4.502	-4.283	6.613	7.430	-196.120	<0.001
500C_plate	2.641	-1.917	3.007	6.303	-88.643	<0.001
600C_plate	-1.753	-2.252	7.960	7.703	-6.487	<0.001
700C_plate	4.539	1.106	8.861	15.144	-35.424	<0.001

(especially 700 °C), however, a large height variation of both the glaze layer and non-glaze layer are observed, which may be resulting from severe plastic deformation of the substrate and possibly local welding at those temperatures before the start of the cycling.

In addition, the count ratio of the glaze layer to non-glaze layer pixels is displayed by the relative size (i.e., covered area) of the two histograms. This count ratio increases with temperature corresponding to an increase in glaze layer coverage with increasing temperature. A more rigorous quantitative analysis on the glaze layer coverage is later conducted in section 5.3.

To determine if the height difference between the glaze and non-glaze layers is statistically significant, a one-tailed unequal variance t-test (Welch's t-test) was conducted. The hypotheses are:

H0. the mean height of glaze and non-glaze layer are the same.

H1. the mean height of glaze layer is higher than that of non-glaze layer.

The unequal variance t-test results are summarized in Table 3. For all temperatures, the null hypothesis is rejected by the low p values, which suggests that the height difference between the glaze and non-glaze layers within wear scar is statistically significant with 99.9% or higher confidence.

Considering the maximum and minimal height within each wear scar, we noticed that the overall minimal height location (i.e., valley) is always occupied by a non-glaze layer. The overall highest location, on the other hand, may still contain other features that are not associated with the glaze layer. For example, the maximum height for 280 °C plate, circled in the OM and height maps in Fig. 9, occurs at the edge of the wear scar resulting from plastic deformation. But locally the glaze layer will always cover the local high locations particularly if the sampling zone is well within the wear scar. The observation that the glaze layer always occupies higher locations within wear scar is probably a result from its tribo-sintering formation mechanism [28–30]. Sintering depends on sufficient temperature and pressure. Wear debris located at a relatively high position has a better chance to be in contact and hence bearing load which drives the sintering process. At the same time, being at a relatively high location may also result in a reduction of the real contact area, which is beneficial for friction and wear reduction for hard bodies like metals. At extreme temperatures (above 600 °C), while glaze layer formation occurs rapidly upon contact, the severe plastic deformation of the bulk can lead to larger variation in relative height, which leads to the large height variance of the adhering glaze layer.

The observed tendency for the glaze layer being in a higher position and hence the surface in contact with the other body is consistent with the classical theory that glaze layer reduces friction and wear by eliminating metal-metal contact [7–9]. Hence, the reduction in friction and wear is likely a combination of the reduction in the real contact area and the reduction in metal-on-metal contact.

5.3. Temperature dependence on the coverage of the glaze layer

The projected glaze layer coverage C_p is given by Ref. [18].

$$C_p = \frac{\text{Area covered by glaze layer}}{\text{Total projected area of wear scar}} \quad (4)$$

Since all images are aligned to the height map that has a constant magnification and identical pixel resolution, Eq. (4) is equivalent to

$$C_p = \frac{N_{\text{glaze}}}{N_{\text{tot}}} = \frac{N_{\text{glaze}}}{N_{\text{glaze}} + N_{\text{non_glaze}}} \quad (5)$$

where N_{tot} is the total number of pixels in a selected wear scar area that covers wear scar region; N_{glaze} and $N_{\text{non_glaze}}$ are the number of pixels labeled as glaze layer or non-glaze layer in the selected area. The glaze layer coverage for both pin and plate from 250 °C to 700 °C are shown in Fig. 3(a). In general, C_p for the pin and plate at each temperature are very similar to each other, and they follow the same trend with increasing temperature. This similarity was expected for like bodies due to the identical chemical and mechanical properties. Although severe-to-mild wear transition appeared as low as 200 °C for the number of cycles applied, a glaze layer was not clearly identified until the temperature reaches 250 °C. The projected glaze layer coverage at 250 °C for both the pin and plate is less than 5%. It is likely that the reduction in wear at 250 °C is mostly attributed to the compacted debris bed that is not fully sintered to have the characteristics of a completely formed glaze layer [12,31]. Towards the temperature where severe-to-mild wear transition is observed by the material response, the projected glaze layer coverage is about 36%. This observation is consistent with others who reported <50% projected coverage is needed to achieve a complete severe-to-mild wear transition [18]. The projected coverage of the glaze layer continuously increases with further temperature rise, and reaches about 75% at the 700 °C, the highest test temperature considered in this work.

Based on the rate change of C_p with respect to the temperature (denoted as \bar{C}_p), the evolution of glaze layer coverage with increasing temperature for the material and test conditions considered can be divided into three stages:

Stage 1 ($T \leq 300$ °C): \bar{C}_p is constant. In other words, C_p increases linearly with temperature increase.

Stage 2 (300 °C < $T \leq 600$ °C): \bar{C}_p increases rapidly with rising temperature.

Stage 3 ($T > 600$ °C): \bar{C}_p increases slowly compared to Stage 2.

It is interesting to observe that the temperature range for the three stages of glaze layer coverage evolution with temperature is well overlay with that of Region II, III and IV in the severe-to-mild transition of friction and wear for the material couple as shown in Fig. 3(a). This observation provides strong evidence that the severe-to-mild transition is induced by the development of glaze layer. It worth emphasizing that the glaze layer coverage determined here is the coverage by 2D projection of the whole wear scar (projected coverage, C_p), not the coverage with respect to the real contact area (real coverage, C_r). The calculation of C_r is similar to Eq. (4) except the denominator should be replaced by the total area that is in contact. Since the height variation within wear scar is one magnitude smaller than the width of wear scar, we ignore the curvature-induced difference between projection area and real contact area. Therefore, the equation for C_r can be approximated by:

$$C_r = \frac{N_{\text{glaze_c}}}{N_{\text{glaze_c}} + N_{\text{non_glaze_c}}} \quad (6)$$

where $N_{\text{glaze_c}}$ and $N_{\text{non_glaze_c}}$ represent the number of glaze layer and non-glaze layer pixels that are in contact, respectively. From the previous discussion we have already identified that the glaze layer is associated with the relatively high locations within the wear scar. At the same time, the tribo-sintering mechanism of the glaze layer formation also requires that the two bodies be in contact in the glaze layer region,

at least at the moment of formation. Thus, it can be assumed that most glaze layers are in contact, i.e., $N_{glaze_c} \approx N_{glaze}$. Non-glaze layer portions, in contrast, will have less possibility to be in contact due to its relatively low height. The portion of non-glaze layer area that is lower than its nearby glaze layer, especially those that are in the small valleys, may not be in contact during the fretting process, which makes $N_{non-glaze_c} < N_{non-glaze}$. As a result, C_r is expected to be higher than C_p for the same wear scar due to its smaller denominator. This explains why the minimum percent of glaze layer coverage upon severe-to-mild transition finishing can be less than 50% in many reported works [17, 18], including in this work (36%), since all reported work are using C_p . The real coverage C_r is expected to be a higher value that is sufficient to alter the overall mechanical properties of the contact surfaces.

On the other hand, the rate difference of glaze layer coverage in the three stages may imply a mechanism change of glaze layer formation and/or its retention. It is believed that glaze layer is formed by a tribosintering of wear debris [5, 28, 32], and removal of wear debris from the interface will result in failure in glaze layer formation [33]. According to Fig. 3(b), the Cof quickly dropped at 700 °C within the first 2000 cycles, which indicates that a sufficient amount of glaze layer has formed at a very early stage of the wear process at this temperature. The protection from the initially formed glaze layer can reduce the supply of fresh wear debris, which may explain the reduction of C_p beyond 600 °C.

5.4. Evaluation of wear characterization tools for glaze layer identification

Having done a deep dive on tools for glaze layer characterization and gained experience on the characteristics of the glaze layer that can be captured by each tool, an overview of the benefits and disadvantages of the various tools can be given to provide a deeper thinking on what makes a good criterion for glaze layer identification.

To better compare the tools used in this and the work of others, it is necessary to set a standard for judging different criteria. Clearly, a good set of criteria should be sufficient to robustly distinguish a glaze layer from a non-glaze layer. High accuracy of glaze layer identification requires that both type I error (mis-identify glaze layer as non-glaze layer, i.e., false negative) and type II errors (mis-identify non-glaze as glaze layer, i.e., false positive) to be low. In addition to accuracy, the choice of the characterization tools can be further optimized to accommodate cost, convenience, availability and redundancy. Determination of the glaze layer identification criteria requires deep understanding of not only glaze layer, but also the characteristics of the non-glaze layer portion of the wear scar.

In the current work, the major source for type I error comes from the wear trace on top of the glaze layer, and it is well controlled by adding the ring light and applying opening/closing operation in image processing. Type II error is more challenging to handle, since some non-glaze layer features share similar characteristics to the glaze layer. Four primary non-glaze layer features have been identified as possible sources of a type II error:

Unworn: This feature describes the reference area that is outside of the wear scar. While it does not participate in the contact and rubbing between the two bodies, it does experience static oxidation process during the test, and will be covered by a thin and uniform oxide layer. Unworn surfaces tend to have a smooth surface morphology and its height is usually set as reference (zero height plane) to normalize height in the profilometer characterization.

Build-up: This wear feature is found at or outside of wear scar edges that is usually highly oxidized and consists of the highest spots of the entire wear region. This feature may result from plastic deformation of the two bodies during reciprocating, expelled large wear particles, or spot-welded wear debris at extreme temperatures. This feature usually has an irregular shape and morphology, but it may appear

dark in SE SEM images either due to charging effect or if it was once in contact with and flattened by the other body. Examples of build-ups are circled in the OM and height maps in Fig. 9.

Embryonic glaze: This feature consists of condensed yet not fully sintered oxide or oxidized debris, and it can be found near the glaze layer region or before the formation of the glaze layer. In an OM image with coaxial illumination lighting mode, this region has a similar hue as a glaze layer, but Its morphology is usually rougher than that of a glaze layer due to incomplete sintering.

Shiny spot: This feature refers to a highly reflective region that is mostly found in valleys of the wear scar. It may be a freshly exposed surface near the end of the test and may also have a statically formed oxide layer.

Table 4 summarizes the major tools and techniques that have been used or could be used to characterize the glaze layer, each of which targets one or more aspect of glaze layer's characteristics. The representation of glaze layer and the four non-glaze layer features are listed under each target characteristics. Possible type II error sources are shaded where the non-glaze layer features identified in each column has similar characteristics to the glaze layer under the same characterization technique. As indicated in this chart, there is always one or more type II error sources if only considering a single feature of glaze layer. Thus, it is essential that any criterion should depend on two or more characteristics to achieve sufficient and robust glaze layer identification. The H-V criterion proposed in this work is an effective one because it involves a single, widely available characterization tool, OM, with no redundancy. With help of Table 4, additional glaze layer identification criteria can be conceived by mixing and matching characterization techniques based on tool availability, and fusing the characterization results with the developed image alignment pipeline.

Table 4 also illuminates that “type of oxide” and “relative height” are not suitable choices to make glaze layer identification criterion. Although the preferred oxide type for glaze layer formation has been widely studied [3, 14, 32, 34–36], those studies were mostly conducted on the pre-identified glaze layer, instead of the other way around utilizing the oxide type information for glaze layer identification. In fact, mapping the type of oxide at a sufficient pixel resolution at large scale can be challenging, especially in cases where multiple types of oxide co-exist in both the glaze layer and non-glaze layer regions (denoted as “various” in the table). Relative height, on the other hand, consist a distribution (as illustrated in Fig. 9) for both glaze layer and non-glaze layer, and does not have a clear cut-off value to differentiate glaze layer and non-glaze layer. So, the relative height is not a suitable quantitative measure for glaze layer identification either.

6. Conclusions

In this work, we developed strategies that enable multi-spectrum study of wear scars. This methodology is applied to study the glaze layer formed on 310S stainless steel after like-on-like, cylinder-on-flat fretting tests at different temperatures, from 20 °C to 700 °C. The key findings and contributions are summarized as below:

1. Computer vision concepts have been introduced to the image analysis of worn surfaces, and a systematic workflow has been established and demonstrated for aligning images captured by various characterization tools with sub-pixel error. In this way the characterization results are integrated to cover multiple characteristics of wear features.
2. We proposed a new quantitative criterion, H-V criterion, for glaze layer identification based the HSV separation of OM images taken using the CXI lighting mode. This method can quickly identify the glaze layer parts of the wear scar in a satisfactorily accurate manner using optical microscopy. The parameters used in the H-V criterion

Table 4

Summary of existing tools that could be used to characterize glaze layer, and the outcome of glaze layer and non-glaze layer feature under those characterization. Possible type II error source(s) for each tool column are highlighted.

Tool candidate(s)	Feature measured	Outcome				
		Glaze layer	Non-glaze layer			
			Unworn	Build-up	Embryonic glaze	Shiny spot
BSE, EDX	O wt%	high	low	low-mid	high	mid
SE, Profilometer	Surface morphology	smooth	smooth	rough or smooth	rough	smooth
OM (with CXI lighting)	Reflection -V value	high	high	low-mid	low	high at low Temp
OM (with CXI lighting)	Color -H value	green-blueish tint	various	various	green-blueish tint	various
Raman, XPS	Type of oxide	various	various	various	various	various
Profilometer	Relative height	local high	zero height plane	overall high	lower than neighbor glaze layer	low
Manual label	Location	within wear scar	outside of wear scar	at the edges of wear scars	within wear scar	within wear scar, mostly in valleys

are very stable regardless of testing temperature, which may imply a constant thickness or composition of glaze layer.

- Using the new tools, we studied the height distribution of glaze layer and non-glaze layer at various testing temperatures and revealed that the glaze layer always occupies relatively high locations within the wear scar. The height difference between the glaze layer and non-glaze layer is statistically significant. This phenomenon may be explained by the tribo-sintering mechanism theory for glaze layer formation. This result also suggests that the glaze layer may reduce friction and wear by reducing the real contact area.
- Both the projected coverage of glaze layer on the pin and that on the plate follow the same increasing trend with temperature rise as the two bodies are the same material. The projected coverage of glaze layer is observed upon finishing severe-to-mild transition is 36%. Three distinct stages of this trend have been discovered and they are well aligned with the severe-to-mild transition of the wear behavior of the tested material system. This observation suggests that the development of glaze layer and its expanding coverage is the key reason for the severe-to-mild wear transition. Given that the glaze layer occupies a higher position within the wear scar, the coverage of the glaze layer with respect to the real contact area is expected to be higher than the projected coverage and high enough to alter the mechanical property of the contact interface.
- Characterization tools that have been used for glaze layer identification and characterization have been compared and evaluated, which enables the conceiving of more customized glaze layer identification criterion based on research goals and tool availability.

Declaration of competing interest

The authors declare that they have no known competing financial interests or personal relationships that could have appeared to influence the work reported in this paper.

Acknowledgement

Wear experiments were conducted in the Mechanical Properties Characterization Facility (MPCF). Profilometer and OM characterization were conducted using facilities from Precision Machining Research

Consortium (PMRC). SEM characterizations of this work were performed in part at the Georgia Tech Institute for Electronics and Nanotechnology (IEN), a member of the National Nanotechnology Coordinated Infrastructure (NNCI), which is supported by the National Science Foundation (ECCS-2025462).

References

- F.H. Stott, High-temperature sliding wear of metals, *Tribol. Int.* 35 (2002) 489–495, [https://doi.org/10.1016/S0301-679X\(02\)00041-5](https://doi.org/10.1016/S0301-679X(02)00041-5).
- D.S. Lin, F.H. Stott, G.C. Wood, The effects of elevated ambient temperatures on the friction and wear behavior of some commercial nickel base alloys, *ASLE Trans* 17 (1974) 251–262, <https://doi.org/10.1080/05698197408981463>.
- T. Kayaba, A. Iwabuchi, The fretting wear of 0.45% C steel and austenitic stainless steel from 20 to 650 °C in air, *Wear* 74 (1981) 229–245, [https://doi.org/10.1016/0043-1648\(81\)90165-4](https://doi.org/10.1016/0043-1648(81)90165-4).
- S.R. Pearson, P.H. Shipway, J.O. Abere, R.A.A. Hewitt, The effect of temperature on wear and friction of a high strength steel in fretting, *Wear* 303 (2013) 622–631, <https://doi.org/10.1016/j.wear.2013.03.048>.
- A. Dréano, S. Fourny, G. Guillonneau, A tribo-oxidation abrasive wear model to quantify the wear rate of a cobalt-based alloy subjected to fretting in low-to-medium temperature conditions, *Tribol. Int.* 125 (2018) 128–140, <https://doi.org/10.1016/j.triboint.2018.04.032>.
- J.K. Lancaster, The formation of surface films at the transition between mild and severe metallic wear, *Proc. R. Soc. London, Ser. A, Math. Phys. Sci.* 273 (1963) 466–483, <https://doi.org/10.1098/rspa.1963.0103>.
- J. Glascott, F.H. Stott, G.C. Wood, The transition from severe to mild sliding wear for Fe-12%Cr-base alloys at low temperatures, *Wear* 97 (1984) 155–178.
- F.H. Stott, J. Glascott, G. Wood, The sliding wear of commercial Fe-12%Cr alloys at high temperature, *Wear* 101 (1985) 311–324.
- J. Glascott, F.H. Stott, G.C. Wood, The effectiveness of oxides in reducing sliding wear of alloys, *Oxid. Metals* 24 (1985) 99–114, <https://doi.org/10.1007/BF00664227>.
- C. Rynio, H. Hattendorf, J. Klöwer, G. Eggeler, The evolution of tribolayers during high temperature sliding wear, *Wear* 315 (2014) 1–10, <https://doi.org/10.1016/j.wear.2014.03.007>.
- A. Viat, G. Guillonneau, S. Fourny, G. Kermouche, S. Sao Joao, J. Wehrs, J. Michler, J.F. Henne, Brittle to ductile transition of tribomaterial in relation to wear response at high temperatures, *Wear* 392–393 (2017) 60–68, <https://doi.org/10.1016/j.wear.2017.09.015>.
- M. Godet, The third-body approach: a mechanical view of wear, *Wear* 100 (1984) 437–452, [https://doi.org/10.1016/0043-1648\(84\)90025-5](https://doi.org/10.1016/0043-1648(84)90025-5).
- L. Vincent, Y. Berthier, A. Floquet, M. Godet, Fretting: load carrying capacity of wear debris, *J. Tribol.* 106 (1984) 192–200, <https://doi.org/10.1115/1.3260881>.
- T.F.J. Quinn, Review of oxidative wear: Part I: the origins of oxidative wear, *Tribol. Int.* 16 (1983) 257–271, [https://doi.org/10.1016/0301-679X\(83\)90086-5](https://doi.org/10.1016/0301-679X(83)90086-5).
- I. García, A. Ramil, J.P. Celis, A mild oxidation model valid for discontinuous contacts in sliding wear tests: role of contact frequency, *Wear* 254 (2003) 429–440, [https://doi.org/10.1016/S0043-1648\(03\)00262-X](https://doi.org/10.1016/S0043-1648(03)00262-X).

- [16] A. Dreano, S. Fouvry, S. Sao Joao, J. Galipaud, G. Guillonneau, S. Sao-Joao, J. Galipaud, G. Guillonneau, The formation of a cobalt-based glaze layer at high temperature: a layered structure, Wear 440–441 (2019) 203101, <https://doi.org/10.1016/j.wear.2019.203101>.
- [17] A. Dréano, S. Fouvry, G. Guillonneau, A combined friction energy and triboxidation formulation to describe the high temperature fretting wear response of a cobalt-based alloy, Wear 426–427 (2019) 712–724, <https://doi.org/10.1016/j.wear.2019.01.023>.
- [18] J. Jiang, F.H. Stott, M.M. Stack, Characterization of wear scar surfaces using combined three-dimensional topographic analysis and contact resistance measurements, Tribol. Int. 30 (1997) 517–526, [https://doi.org/10.1016/S0301-679X\(96\)00074-6](https://doi.org/10.1016/S0301-679X(96)00074-6).
- [19] F.H. Stott, D.S. Lin, G.C. Wood, The structure and mechanism of formation of the 'glaze' oxide layers produced on nickel-based alloys during wear at high temperatures, Corrosion Sci. 13 (1973) 449–469.
- [20] W.M. Rainforth, A.J. Leonard, C. Perrin, A. Bedolla-Jacuinde, Y. Wang, H. Jones, Q. Luo, High resolution observations of friction-induced oxide and its interaction with the worn surface, Tribol. Int. 35 (2002) 731–748, [https://doi.org/10.1016/S0301-679X\(02\)00040-3](https://doi.org/10.1016/S0301-679X(02)00040-3).
- [21] C. Rynio, H. Hattendorf, J. Klöwer, G. Eggeler, On the physical nature of tribolayers and wear debris after sliding wear in a superalloy/steel tribosystem at 25 and 300°C, Wear 317 (2014) 26–38, <https://doi.org/10.1016/j.wear.2014.04.022>.
- [22] X. Jin, P.H. Shipway, W. Sun, The role of temperature and frequency on fretting wear of a like-on-like stainless steel contact, Tribol. Lett. (2017), <https://doi.org/10.1007/s11249-017-0858-0>.
- [23] R. Hartley, A. Zisserman, *Multiple View Geometry in Computer Vision*, Cambridge university press, 2003.
- [24] R. Szeliski, *Computer Vision: Algorithms and Applications*, Springer Science & Business Media, 2010.
- [25] C. Zhang, *Wear Rate and Mechanism Maps for Stainless Steel at High Temperature*, Georgia Institute of Technology, 2020.
- [26] D.J. Whitehouse, *Handbook of Surface Metrology*, CRC Press, 1994.
- [27] N. Efford, *Digital Image Processing: A Practical Introduction Using JavaTM*, Pearson Education, Slate, 2000.
- [28] K. Adachi, K. Kato, Formation of smooth wear surfaces on alumina ceramics by embedding and tribo-sintering of fine wear particles, Wear 245 (2000) 84–91.
- [29] A. Dreano, S. Fouvry, G. Guillonneau, Understanding and formalization of the fretting-wear behavior of a cobalt-based alloy at high temperature, Wear 452–453 (2020) 203297, <https://doi.org/10.1016/j.wear.2020.203297>.
- [30] C.H. Hager, J. Hu, C. Muratore, A.A. Voevodin, R. Grandhi, The mechanisms of gross slip fretting wear on nickel oxide/Ti6Al4V mated surfaces, Wear 268 (2010) 1195–1204, <https://doi.org/10.1016/j.wear.2009.11.004>.
- [31] L. Vincent, Y. Berthier, A. Floquet, M. Godet, Fretting: load carrying capacity of wear debris, J. Tribol. 106 (1984) 192–200, <https://doi.org/10.1115/1.3260881>.
- [32] H. Kato, K. Komai, Tribofilm formation and mild wear by tribo-sintering of nanometer-sized oxide particles on rubbing steel surfaces, Wear 262 (2007) 36–41.
- [33] E.R. Leheup, R.E. Pendlebury, Unlubricated reciprocating wear of stainless steel with an interfacial air flow, Wear 142 (1991) 351–372, [https://doi.org/10.1016/0043-1648\(91\)90174-S](https://doi.org/10.1016/0043-1648(91)90174-S).
- [34] A. Viat, A. Dréano, S. Fouvry, M.I. De Barros Bouchet, J.F. Henne, Fretting wear of pure cobalt chromium and nickel to identify the distinct roles of HS25 alloying elements in high temperature glaze layer formation, Wear 376–377 (2017) 1043–1054, <https://doi.org/10.1016/j.wear.2017.01.049>.
- [35] P.L. Hurricks, The fretting wear of mild steel from 200° to 500°C, Wear 30 (1974) 189–212.
- [36] P.L. Hurricks, The fretting wear of mild steel from room temperature to 200°C, Wear 19 (1972) 207–229, [https://doi.org/10.1016/0043-1648\(72\)90304-3](https://doi.org/10.1016/0043-1648(72)90304-3).